University of Birmingham

All-Metal Phased Array with Full Polarization Reconfigurability

Sun, Liying; Lu, Yunlong; Xu, Lintong; You, Yang; Xu, Jun; Wang, Yi; Huang, Jifu

Link to publication on Research at Birmingham portal

All-Metal Phased Array with Full Polarization Reconfigurability

Liying Sun, Yunlong Lu, *Member, IEEE*, Lintong Xu, Yang You, Jun Xu, *Member, IEEE*, Yi Wang, *Senior Member, IEEE*, and Jifu Huang

Abstract—**An all-metal phased array with full polarization reconfigurability is presented in this paper. Septum polarizers as phased array elements are first used to achieve left-handed and right-handed circular polarizations (LHCP and RHCP), and arbitrary linear polarizations (LPs) can be further synthesized. Two pairs of metal ridges are loaded into the septum polarizer to reduce the profile and aperture size, so that the spacing between the two adjacent array elements can be constrained to about half of the free-space wavelength at the center operating frequency.** **Phased arrays of 1 × 8 and 8 × 8 elements covering 25.5 - 27 GHz are designed to demonstrate the 1-D and 2-D beam scanning performance with different polarizations. For demonstration, the 1 × 8-element phased array is implemented.** **Experimental results show that the array exhibits stable beam scanning performance for both CPs and LPs. The synthesized beam scanning range is up to ±55° with a gain-reduction of 4.7 dB for all polarizations. Under beam scanning, the axial ratio (AR) remains below 3.1 dB for the LHCP and RHCP, and the maximum gain variation during polarization reconfiguration is less than 0.8 dB.**

Keywords—**Phased array, beam scanning, septum polarizer, polarization reconfigurability.**

I. INTRODUCTION

Phased arrays are widely used in radars [1]-[3], satellite communications [4]-[6], and the fifth-generation (5G) millimeter-wave (mmW) mobile communications [7]-[9]. Introducing polarization reconfigurability into the phased array can improve the performance and capability of the wireless system [10]-[12]. For example, it can enhance the target acquisition ability of a radar or improve the channel capacity and anti-multipath fading ability of a wireless communication system.

An array element with dual-polarization operation, such as orthogonal linear polarizations (LPs) or orthogonal circular polarizations (CPs), is the key component in a full-polarization phased array. Various dual-polarized elements have been demonstrated, including patches [13]-[15], cross-shaped dipoles [16], [17], and magneto-electric dipoles [18]-[20]. Full polarization reconfiguration can be subsequently realized by controlling the amplitude and phase differences between the dual excitations [21]-[24]. However, the aforementioned works are based on microstrip transmission lines or substrate-integrated waveguides. When the operating frequency rises to mmW bands, the dielectric loss will cause a significant drop in antenna efficiency. Air-filled all-metal phased arrays can be a solution. Moreover, for high power applications, the all-metal antenna structure can be used as a heat sink to dissipate heat.

All-metal dual-polarized array elements, however, usually suffer from relatively large volumes, which poses a challenge in meeting the spacing requirement of a phased array. Some all-metal dipoles are miniaturized to meet this requirement [25], [26]. A cross-shaped dipole loaded with vertically bent metal plates is presented in [26] for a dual-LP wide-angle scanning phased array in the frequency of 4.4 - 5 GHz. The element spacing is reduced to $0.47\lambda_0$ (λ_0 is the free-space wavelength at the center frequency). This enables a wide beam scanning rang of over ±60° for both LPs. However, due to its complex element structure, it is difficult to be scaled for mmW applications. Some simple all-metal end-fire antennas have also been used to construct dual LP phased arrays, typically with Vivaldi antennas [27]-[30]. A dual LP configuration can be achieved by orthogonally placing the Vivaldi antennas. However, the high antenna profile and polarization degradation during wide-angle scanning in the non-principal planes are the main drawbacks [31], [32]. [33] presents a dual LP all-metal phased array based on a low-profile frequency-scaled ultra-wideband element. It overcomes some of the disadvantages in the Vivaldi-based phased array, but requires multiple manufacturing techniques, such as computer numerical control (CNC) machining and wire-based electrical discharge machining (wire-EDM). This increases the difficulty in implementation. In addition, the beam scanning performance for other polarizations, such as dual CPs and ±45°-LP, has not been explored in these works. How to achieve an easy-to-manufacture and low-profile mmW all-metal phased array with

Liying Sun, Yunlong Lu, Lintong Xu, Yang You, and Jifu Huang are with the Faculty of Electrical Engineering and Computer Sciences, Ningbo University, Ningbo, Zhejiang, 315211, China (e-mail: luyunlong@nbu.edu.cn).

Jun Xu is with the State Key Laboratory of Millimeter Waves, School of Information Science and Engineering, Southeast University, Nanjing, 210096, P. R. China.

Yi Wang is with School of Engineering, University of Birmingham, B15 2TT, United Kingdom (e-mail: y.wang.1@bham.ac.uk).
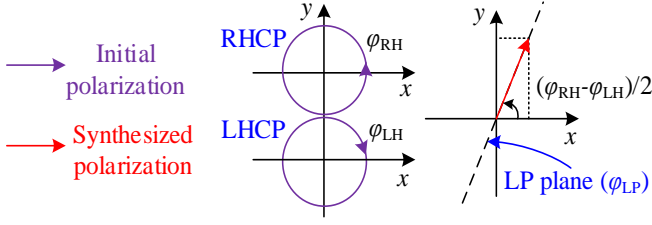
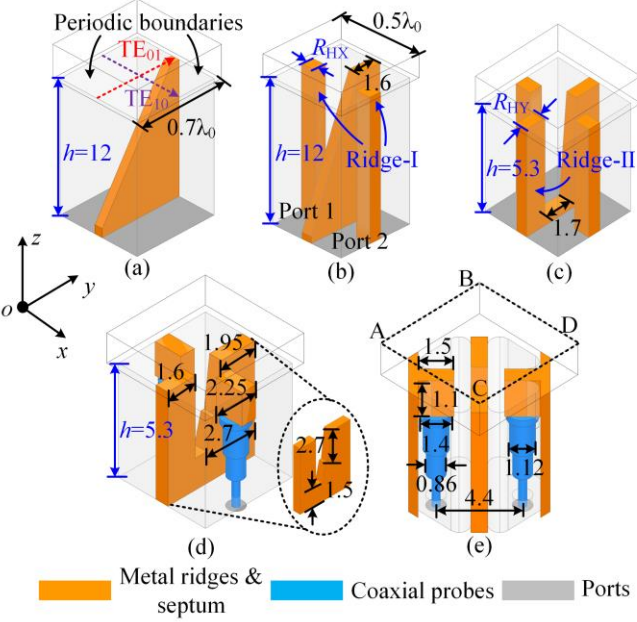Fig. 1. Polarization conversion from orthogonal CPs to arbitrary LPs.

Fig. 2. Design evolution. (a) Conventional septum polarizer; (b) Ridge-I loaded septum polarizer; (c) Ridge-I and Ridge-II loaded septum polarizer; (d) probe excited septum polarizer; (e) 45° rotated septum polarizer. All dimensions are given in millimeters.

full polarization reconfigurability remains a challenge.

In this paper, septum polarizers as phased array elements are used to generate left-handed and right-handed CPs (LHCP and RHCP). Subsequently, arbitrary LPs can be synthesized by simultaneously providing different excitations for the two chirality of CPs. Conventional septum polarizer commonly suffers from its large aperture size and high profile. This makes it difficult to be directly used in phased arrays. The main novel feature of this work is the design of a low-profile miniaturized septum polarizer. This is achieved by loading two pairs of metal ridges into the septum polarizer. Both the profile and the aperture size are reduced to about $0.5\lambda_0$. Therefore, the spacing requirement of a phased array can be satisfied. Two phased arrays of 1×8 and 8×8 elements are proposed to verify the design concept. The remaining parts of this paper are organized as follows: Section II describes the phase array element performance. In Section III, the performance of two differently scaled phased arrays is exhibited and discussed, followed by a conclusion in Section IV.

II. PHASED ARRAY ELEMENT

Most wireless systems rely on LP or CP electromagnetic (EM) waves. A phased array with reconfigurable polarizations

will make it flexible for various application scenarios. The conversion between different polarizations can start either from the orthogonal CPs or the orthogonal LPs. Most of the previous works utilize orthogonal LPs to achieve the polarization conversion, since dual LP antennas are relatively easier to implement than dual CP antennas. To convert LP to CP, only the phase difference between the orthogonal LPs is controlled. However, when the conversion between different LPs is concerned, this approach would need the precise control of the amplitude and phase of the excitation signals. This increases the complexity of the beam control network of transmitting/receiving (T/R) components [21]-[24].

In contrast, starting with orthogonal CPs avoids this problem. Fig. 1 illustrates the conversion from RHCP and LHCP to arbitrary LPs. It requires equal-amplitude and different phases (φ_{RH} and φ_{LH}) for the RHCP and LHCP, so amplitude control is more readily attainable. The direction of the synthesized LP plane (φ_{LP}) is determined by the phase difference ($\varphi_{RH}-\varphi_{LH}$)/2 [34]. Under this circumstance, an array element with good LHCP and RHCP performance is essential to achieve the full polarization reconfigurability.

Septum polarizer operating at 25.5 - 27 GHz band is adopted in this design. All simulation results are obtained from ANSYS HFSS. The conventional septum polarizer (initial structure) marked with the direction of fundamental modes (TE_{10} and TE_{01}) is shown in Fig. 2(a). Typically, it has a relatively large footprint and profile: (i) the aperture width should be large enough to keep the cut-off frequency of the waveguide away from the passband (usually about $0.7\lambda_0$); (ii) the height is around $1.05\lambda_0$ to ensure a good AR [35]-[37]. The large width of the polarizer would lead to a significant deterioration of the beam scanning capability if used in a phased array. Normally, the element spacing should be about $0.5\lambda_0$ for the beam-scanning phased array [38]. For miniaturization, a pair of metal ridges (Ridge-I) are added to the septum polarizer along the x-direction to reduce its aperture size to $0.5\lambda_0$, as shown in Fig. 2(b). Its cut-off frequency is further controlled by adjusting the ridge height (R_{HX}). Fig. 3 plots the cut-off frequency as a function of the height. Periodic boundaries are applied in simulation to represent the mutual coupling in phased arrays. When R_{HX} is over 1.3 mm, the cut-off frequency is sufficiently away from the passband. The dimensions of the septum after optimization are also given in Fig. 2(b).

To generate the CP wave, the amplitudes and phases of the TE_{01} mode in the septum polarizer along the y-direction and the TE_{10} mode along the x-direction at the position of the radiation aperture should satisfy: $|E_D| = |E_y| - |E_x| = 0$ dB (amplitude condition) and $\angle E_D = \angle E_y - \angle E_x = \pm 90°$ (phase condition). Under the reduced aperture width, the amplitude and phase responses are shown in Fig. 4. Due to symmetry, only the results for port 1 (RHCP) excitation are given. It can be found that the amplitude and phase conditions can only be guaranteed when the polarizer height is sufficient, i.e., 12 mm ($1.05\lambda_0$). Next, we will discuss how to reduce the profile height, which is directly linked to the phase condition.
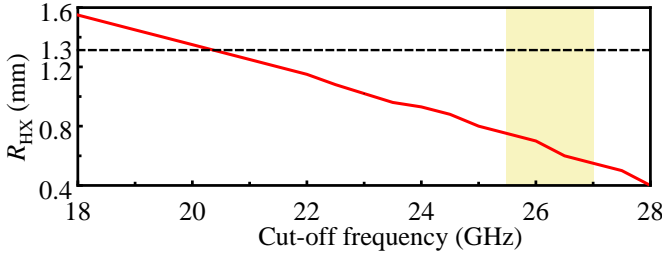
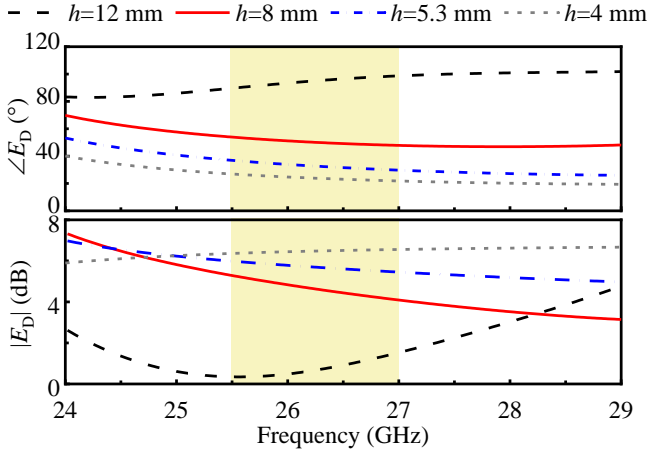Fig. 3. Cut-off frequency of the Ridge-I loaded septum polarizer in Fig. 2(b) with different values of R_{HX}.

Fig. 4. Amplitude and phase differences between the TE_{01} and the TE_{10} modes over the septum polarizer aperture in Fig. 2(b).
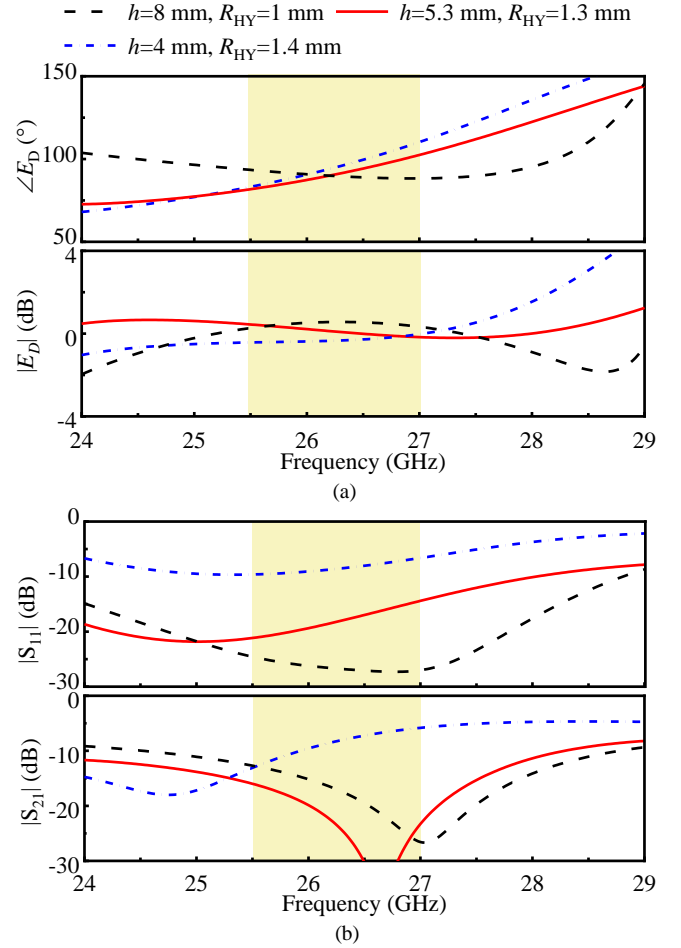

Fig. 5. Simulated results of septum polarizer in Fig. 2(c). (a) Amplitude and phase differences between the TE_{01} and the TE_{10} modes over the septum polarizer aperture; (b) S-parameters.

The phase difference $\angle E_D = \angle E_y - \angle E_x$ at the radiation aperture can be derived by [39]:

$$\angle E_D = \left(\beta_y - \beta_x \right) \times h \qquad (1)$$

where β_y and β_x are the phase constants of the TE_{01} and TE_{10} modes. To reduce the profile height (h) while maintaining the phase difference of 90° (assuming port 1 is excited), we can increase the value of the term (β_y - β_x). This can be achieved by either increasing β_y or decreasing β_x. As we know, the phase constant in the guided-wave structure can be expressed by [39]:

$$\beta = \frac{2\pi \times \sqrt{1 - \left(\frac{\lambda}{\lambda_c} \right)^2}}{\lambda} \qquad (2)$$

where λ is the free-space wavelength, and λ_c is the cut-off wavelength, so β can be controlled by altering λ_c. This can be realized by loading metal ridges to the septum polarizer. Since a pair of ridges have already been added along the x-direction (see Fig. 2(b)), it is difficult to change β_x further. So, we have modified the spectrum along the y-direction with another pair of ridges (Ridge-II), as shown in Fig. 2(c). By increasing its height (R_{HY}), the cut-off frequency is decreased and therefore its cut-off wavelength and β_y of the TE_{01} mode increased. In addition, the Ridge-II pair perturb the E-field distribution of the TE_{01} mode, which compensates the amplitude difference ($|E_D|$) caused by the profile reduction. This allows the septum polarizer to fulfill the amplitude and phase conditions at a significantly reduced height. Fig. 5(a) plots the amplitude and phase differences ($|E_D|$ and $\angle E_D$) at the radiation aperture of septum polarizer with different ridge and profile heights. It can be seen that the R_{HY} can be optimized for different profile heights. Noted that $|S_{21}|$ is the port isolation between the two input ports (for generating different CPs) in a septum polarizer. It can be observed that the input impedance matching and isolation deteriorate when the profile height is less than 4 mm ($0.35\lambda_0$), as shown in Fig. 5(b). Taking the CP characteristics, impedance matching and polarization port isolation into account, a profile height of 5.3 mm ($0.46\lambda_0$) is chosen in this design.

Then, we will explain some practical considerations in designing the excitation ports of the septum polarizer. For phased arrays, the arrangement of the excitation ports needs to be constrained within the footprint of the array element. This is 2.2 mm × 5.1 mm for one port. Such a small footprint cannot accommodate a waveguide port. Therefore, a coaxial probe is used for excitation in this design. The input port at the bottom of the septum polarizer is a male sub-miniature push-on (SMP) structure with a diameter of 0.3 mm. For testing or practical usage, cables with a female SMP connector can be utilized. Fig. 2(d) shows the probe excitation structure. Two multi-stage stepped probes are inserted into the polarizer to connect to the
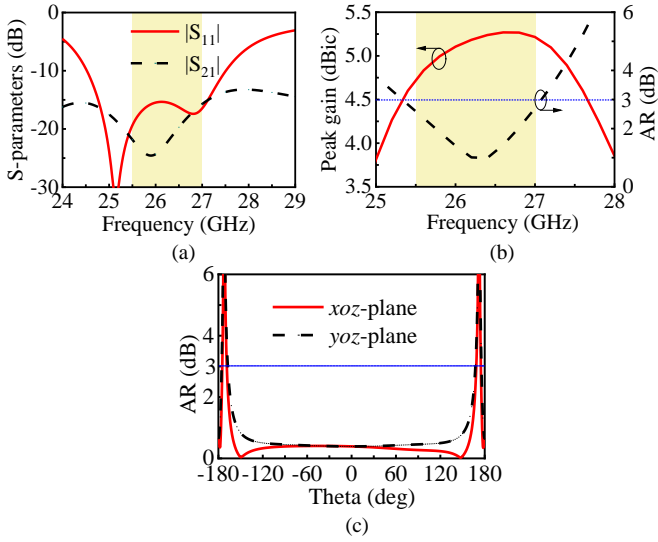
Fig. 6. Simulated RHCP performance of the final septum polarizer (in Fig. 2(e)). (a) S-parameters; (b) peak gain and AR; (c) CP beamwidth at center frequency (26.25 GHz).
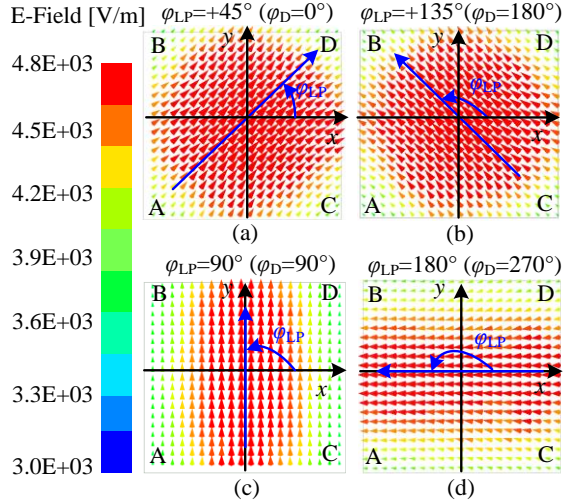

Fig. 7. E-field distribution at the septum polarizer aperture at 26.25 GHz. (a) +45°-pol; (b) -45° (or +135°)-pol; (c) 90°-pol; (d) 0° (or 180°)-pol. (φ_{LP} = (φ_{RH}-φ_{LH})/2+45°, φ_D=φ_{RH}-φ_{LH})

Ridge-I, excite the RHCP at port 1 and the LHCP at port 2. The septum is re-designed into a stepped structure to improve the input impedance matching. To increase the spacing between the two input ports, the Ridge-I and II, as well as the excitation probe, are rotated by 45°, as shown in Fig. 2(e). The spacing is increased to 4.4 mm, enough to place two SMP connectors. It is worth noting that rounded corners are used in Fig. 2(e) to facilitate fabrication. The optimized dimensions of the final septum polarizer are given in Fig. 2(d) and (e).

Fig. 6 shows the simulated S-parameters and radiation performance of the miniaturized septum polarizer for RHCP. The mutual coupling between the adjacent elements for array applications is also considered in the simulation by using periodic boundary conduction. Over the frequency range of 25.5 - 27 GHz, the reflection coefficient is below -15.2 dB and the polarization port isolation between the two input ports of the same septum polarizer is higher than 15.8 dB, as shown in Fig. 6(a). Fig. 6(b) and 6(c) show the radiation performance.
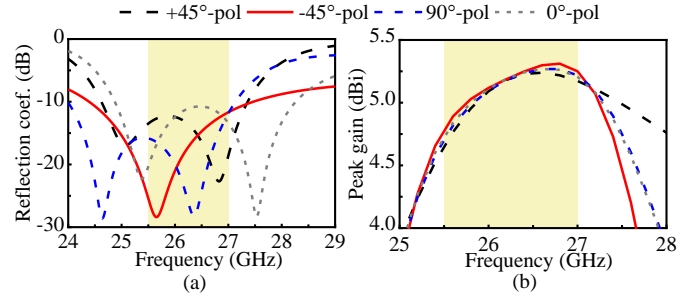
Fig. 8. Simulated results of the final septum polarizer (in Fig. 2(e)) for different LPs. (a) Reflection coefficients; (b) peak gain.
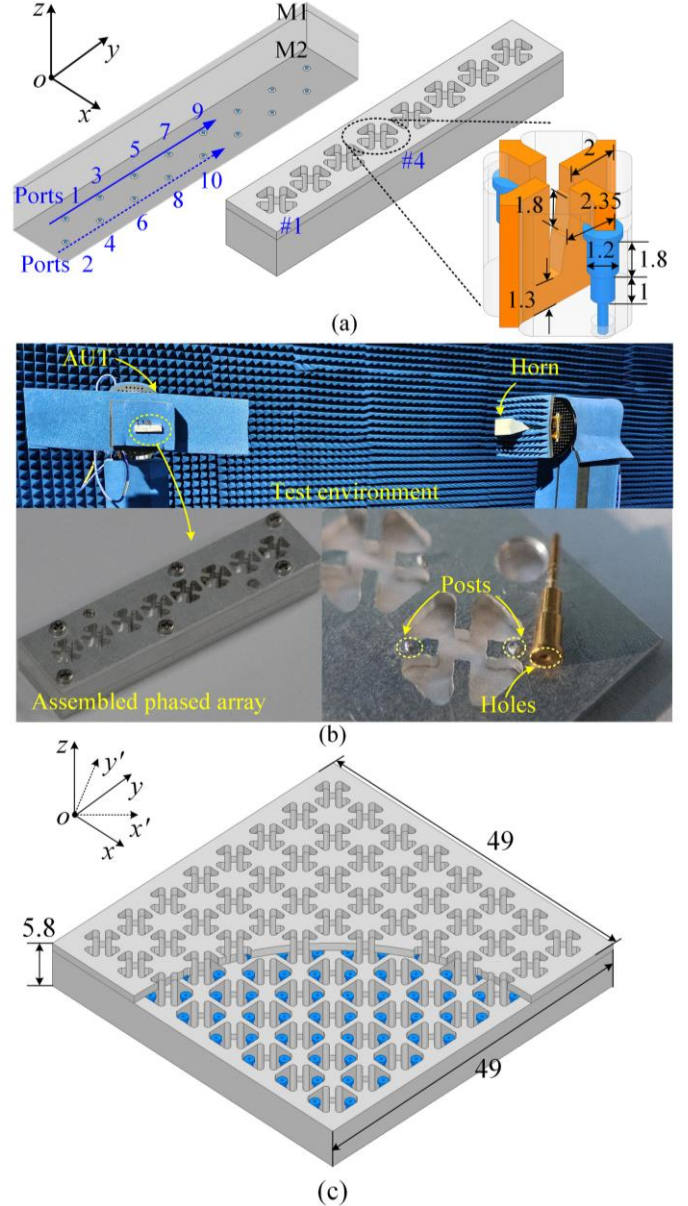
Fig. 9. (a) Structure of the 1×8-element liner phased array; (b) photographs of the assembled prototype and test environment, (c) structure of the 8×8-element planar phased array. All dimensions are given in millimeters.

The peak gain is higher than 4.8 dBic and the AR is within 3 dB across the same frequency range. A wide beamwidth (AR < 3 dB) that covers -158° to +158° in both *xoz*- and *yoz*-planes at
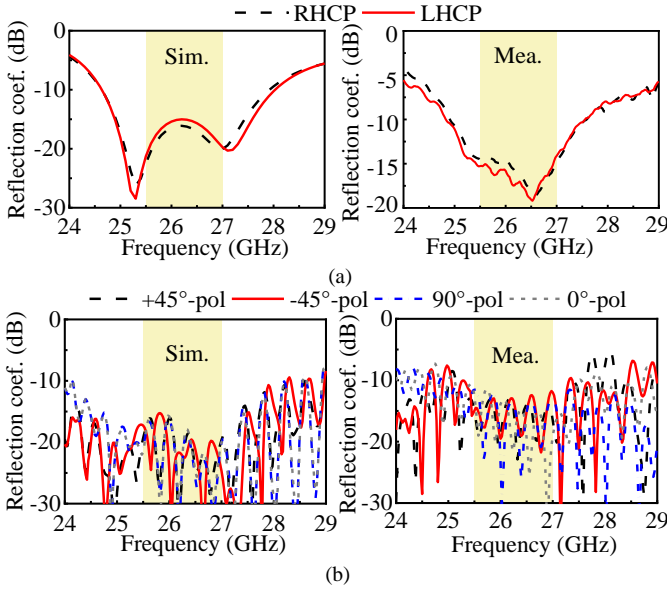
Fig. 10. Simulated and measured reflection coefficients of element #1 in the 1×8-element linear phased array. (a) RHCP and LHCP; (b) different LPs.

Fig. 11. Simulated and measured reflection coefficients of element #4 in the 1×8-element linear phased array. (a) RHCP and LHCP; (b) different LPs.

the center frequency of 26.25 GHz is observed. The same performance is expected when port 2 (LHCP) is excited.

Arbitrary LPs are synthesized by exciting the two ports of the septum polarizer with appropriate phase differences. Four typical LPs, *i.e.*, +45°-pol, -45° (or +135°)-pol, 90°-pol and 0° (or 180°)-pol, are analyzed. Fig. 7 shows the E-field distributions at the radiation aperture (ABCD-plane in Fig. 2(e)) at 26.25 GHz, indicating the expected LPs. The required phase differences (φ_D) between the two excitation ports for the different LPs and the definition of the LP planes (φ_{LP}) are also marked out in Fig. 7. As mentioned previously, the septum polarizer is rotated by 45° (see Fig. 2(e)). This has been considered in devising the phase differences as (φ_{RH}-φ_{LH})/2 + 45° rather than (φ_{RH}-φ_{LH})/2. The simulated reflection coefficients for different LPs are plotted in Fig. 8(a). It should be noted that the reflection coefficients for the four different LPs are obtained when the two input ports of the septum polarizer are excited at the same time. They are all below -11 dB over the frequency range of 25.5 - 27 GHz. The simulated peak gain is shown in Fig. 8(b). Stable and consistent gain for different LPs can be observed, and the value varies within 4.7 - 5.3 dBi, which is similar to the gain of the RHCP and LHCP. The proposed low-profile miniaturized septum polarizer supports full polarization reconfigurability and is suitable for planar phased array applications.

III. PHASED ARRAY PERFORMANCE

A. 1×8-Element Liner Phased Array

The configuration of the 1×8-element linear phased array based on the low-profile miniaturized septum polarizer is shown in Fig. 9(a). The spacing between the adjacent elements is 0.5λ₀. Because there is no mutual coupling along the *x*-direction for the 1D array, the dimensions of the septum polarizer are slightly different from the model discussed in Section II (see Fig. 2(d) and (e)). These are given in Fig. 9(a).
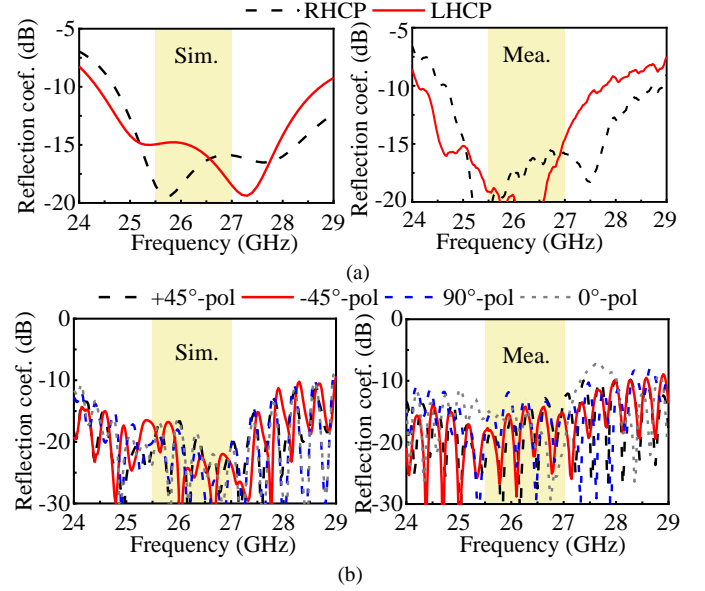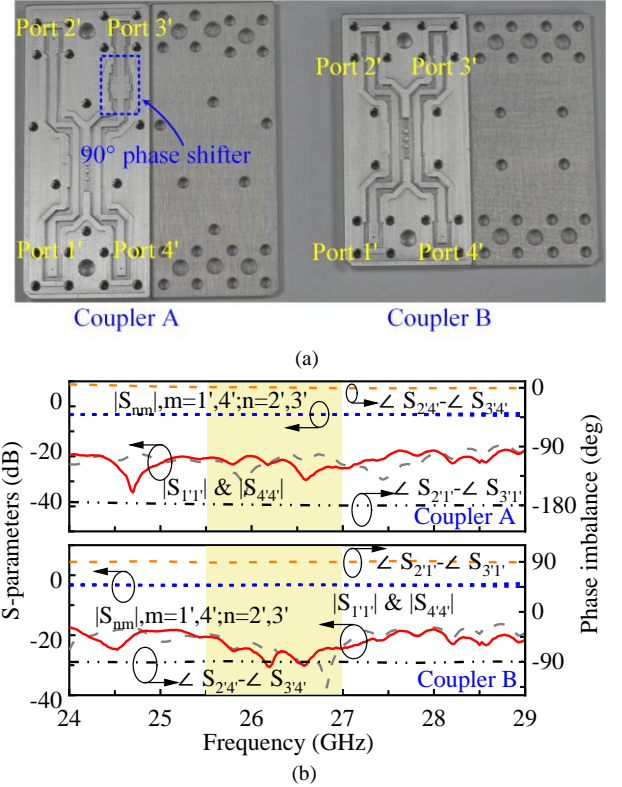
Fig. 12. Fabricated couplers. (a) Photograph; (b) measured S-parameters (port 1' and port 4' in each coupler are excited for measurement).

For validation, a prototype is implemented. It is formed of two metal blocks (M1 and M2) as depicted in Fig. 9(a) and milled out of aluminum-magnesium alloy with a machine tolerance of 20 μm. The nominal conductivity of the aluminum-magnesium alloy used in the simulation is 3.8×10^7 S/m. Screws are used to assemble the antenna and suppress potential leakage. The photographs of the assembled linear phased array and test environment are shown in Fig. 9(b). The small holes of the input probes and matching metal posts on the ridges are
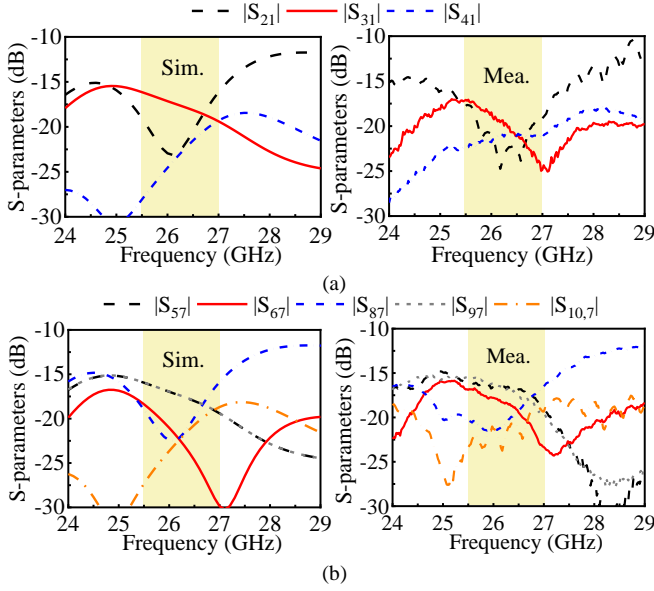
Fig. 13. Simulated and measured port isolation for (a) element #1 and (b) element #4 in the 1×8-element linear phased array.
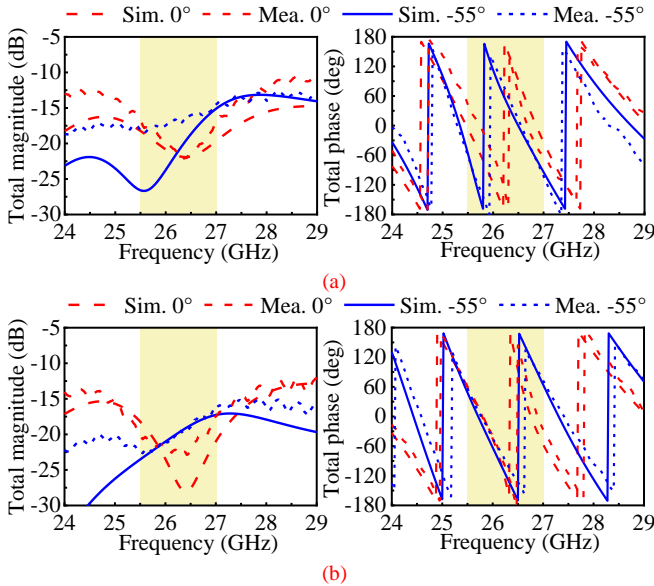
Fig. 14. Simulated and measured active polarization isolation for (a) element #1 and (b) element #4 in the 1×8-element linear phased array.

machined to ensure the accurate positioning of the probe during antenna assembly. The enlarged view of the fabricated probe and metal ridge is shown in Fig. 9(b). The overall size of the fabricated phased array is 14 mm × 51.4 mm × 6.1 mm.

1) Array Element Results

The edge element #1 and center element #4 are chosen as the representatives to present the results. The corresponding excitation ports are ports 1 & 2 and 7 & 8. The simulated and measured reflection coefficients for the two elements are shown in Figs. 10 and 11. The measured results are obtained by using an Agilent E8361C network analyzer. A good agreement is achieved between the simulations and measurements. Note that the reflection coefficients with simultaneous excitation of the input ports of each element are used for the LP cases. In the measurement, two couplers with different phase differences are

used to test the reflection coefficients in the LP configuration. Coupler A provides 0° and 180° phase difference, while coupler B generates 90° and 270° phase difference. Photograph of the couplers and the measured S-parameters are shown in Fig. 12. The desired amplitude and phase responses for each coupler are obtained (see Fig. 12(b)). From Figs. 10 and 11, it can be seen that the measured reflection coefficients of the antenna elements #1 and #4 are all less than -10.8 dB for both the CP and LP cases. It should be noted that the simulated and measured results for the LPs both include the contribution from the broadband couplers. The ANSYS Circuit simulator is used to obtain the simulated results by interconnecting the coupler and the linear phased array with coaxial lines of the same length as for measurement. Fig. 13 shows the simulated and measured port isolation between the input port and adjacent ports. For simplicity, only one of the two input ports is considered. The measured port isolation for both antenna elements #1 and #4 exceeds 15.5 dB over the same frequency band.

Since the linear phased array supports the initial dual polarizations of RHCP and LHCP, the polarization isolation of a specific element including the mutual coupling from the other different-polarized elements should be discussed. For convenience, it is referred to here as active polarization isolation. According to [40], the active polarization isolation of the m-th element can be estimated by exciting one polarization of this element as the receiver and the orthogonal one of all elements as the transmitters. It can be calculated by

$$H_m(\theta) = \sum_{i=1}^{N} S_{m,i} e^{jk(m-i)p\sin\theta} \qquad (3)$$

Here, the $S_{m,i}$ is the passive S-parameters between the element m and i in its complex form. Elements m and i refer to the transmitting and receiving antennas that operate at different polarizations. N is the total number of the elements, k is the wavenumber, p is the spacing between the adjacent elements, and θ is the beam scanning angle. The active polarization isolation for elements #1 and #4 are shown in Fig. 14. Considering the structural symmetry, only the case that element #1 (or #4) operating in RHCP is analyzed. The measured active polarization isolation for elements #1 and #4 is better than 16.8 dB and 17.4 dB at the beam pointing of 0°. When the beam scans to -55°, it is still better than 14.5 dB (element #1)/ 16.2 dB (element #4).

The active reflection coefficient for the m-th element can be calculated by [41]:

$$\Gamma_m(\theta) = \sum_{n=1}^{N} S_{m,n} e^{jk(m-n)p\sin\theta} \qquad (4)$$

where $S_{m,n}$ is still the passive S-parameter in its complex form. Different from Eq. (3), the elements m and n are in the same polarization. With the simulated and measured passive S-parameters of each element (including the couplers for the LP cases), the calculated active voltage standing wave ratio (VSWR) for the edge element #1, and the center element #4, are
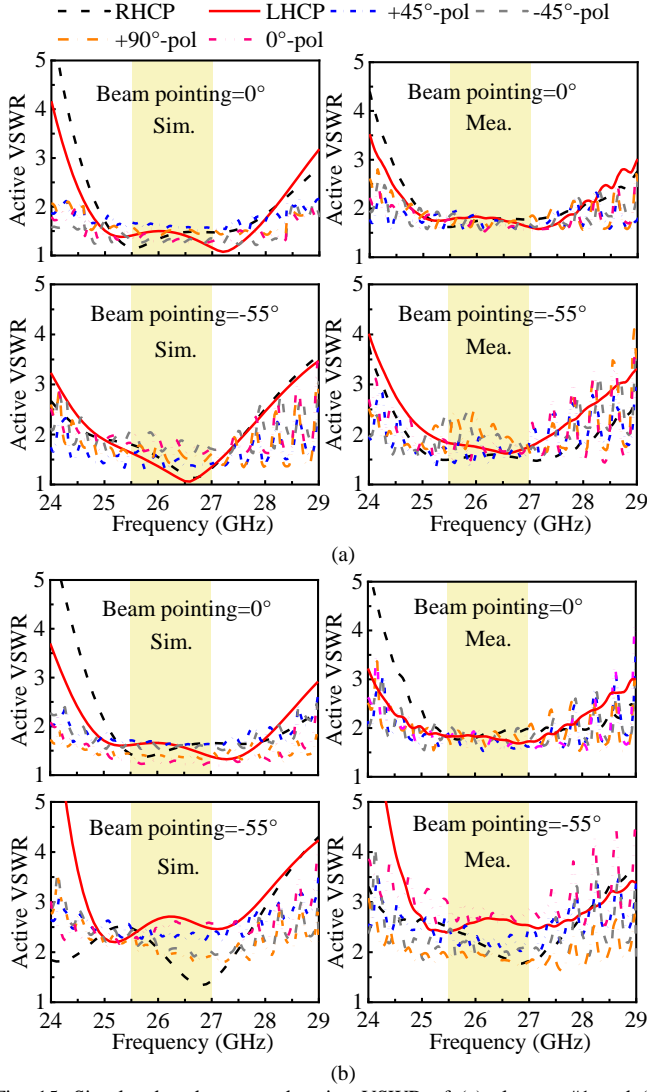
Fig. 15. Simulated and measured active VSWR of (a) element #1 and (b) element #4 in the 1×8-element linear phased array.

plotted in Fig. 15. Due to the increasing mutual coupling, the active VSWR deteriorates at wide beam scanning angles. This is expected as this design is not optimized for wide-angle impedance matching. Except for an active VSWR of 3.0 for the element #4 with 0°-pol at beam scanning angle of -55°, all other active VSWRs are less than 2.7 in the frequency range of 25.5 - 27 GHz. The difference between the simulated and measured results is mainly caused by the errors in manufacturing and experiment.

Figs. 16 and 17 illustrate the simulated and measured radiation patterns of elements #1 and #4 in *yoz*-plane with different polarization configurations. The measured results are obtained by using a far-field antenna test system in an anechoic chamber. A reasonable agreement between the simulations and measurements is achieved. The initial CP radiation patterns are obtained by exciting ports 1/7 (RHCP) and 2/8 (LHCP). The measured 3-dB beamwidth in *yoz*-planes is larger than 94°. Within this beamwidth, the AR remains below 2.5 dB. The measured peak gain of element #1 is larger than 5.6 dBic for both LHCP and RHCP, and it is larger than 5.1 dBic for
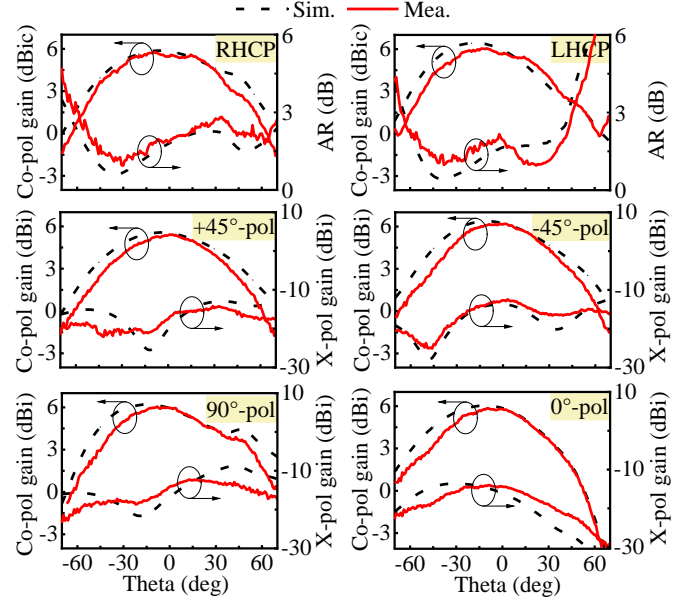
Fig. 16. Simulated and measured radiation performance of element #1 in the 1×8-element linear phased array at 26.25 GHz.
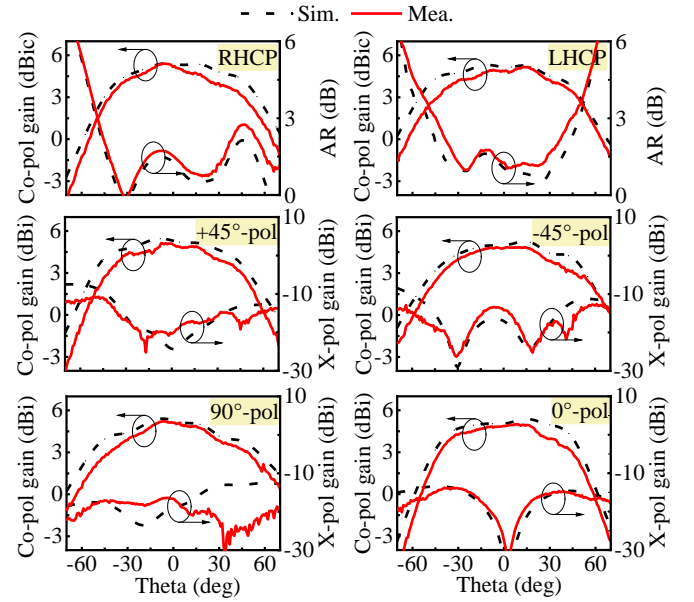
Fig. 17. Simulated and measured radiation performance of element #4 in the 1×8-element linear phased array at 26.25 GHz.

element #4. With reference to the simulated and measured LP radiation patterns in Figs. 16 and 17, it can be seen that stable radiation patterns are also achieved when different LPs are constructed. Values of the measured peak gain for elements #1 and #4 are around 5.3 dBi and 4.8 dBi, respectively, and the variations are slight for different LP states. The 3-dB beamwidths exceed 84° for all LPs, and the cross-polarization discriminations (XPDs) are all better than 18.4 dB within the 3-dB beamwidths.

2) Beam Scanning Performance

Figs. 18 and 19 show the simulated and synthesized 1-D beam scanning performance for different polarizations in the *yoz*-plane at 26.25 GHz. The synthesized results are obtained
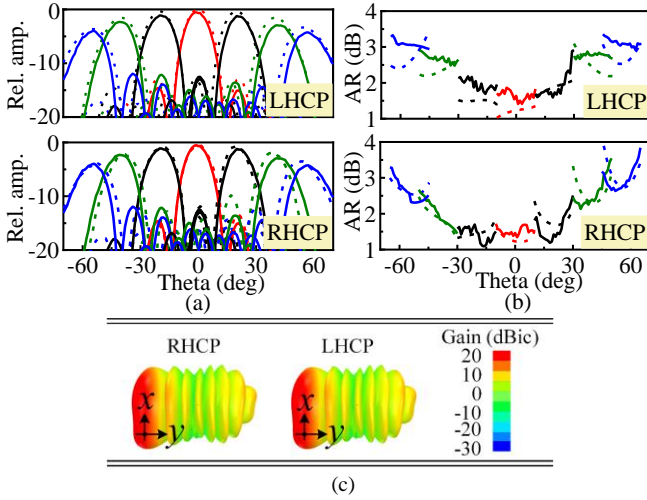
Fig. 18. CP beam scanning of the 1×8-element linear phased array at 26.25 GHz (unit of relative amplitude: dB): (a) Co-pol; (b) AR; (c) top view of 3-D radiation pattern. (Short dash line: simulated results; solid line: synthesized results based on measured AEPs).
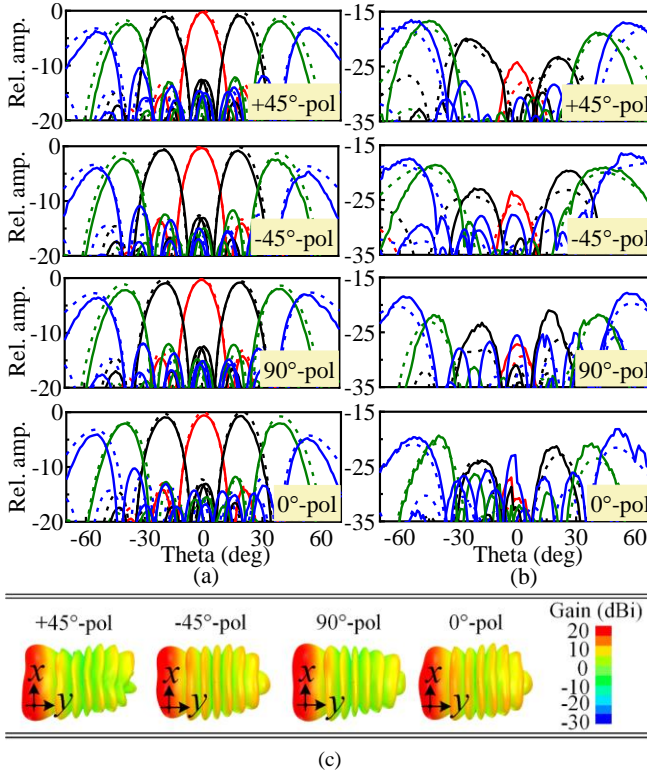
Fig. 19. LP beam scanning of the 1×8-element linear phased array at 26.25 GHz (unit of relative amplitude: dB): (a) Co-pol; (b) X-pol; (c) top view of 3-D radiation pattern. (Short dash line: simulated results; solid line: synthesized results based on measured AEPs).

Fig. 20. Simulated and synthesized antenna peak gain of the 1×8-element linear phased array at different frequencies (unit of gain: dBic/dBi). (a) Simulated results; (b) synthesized results.
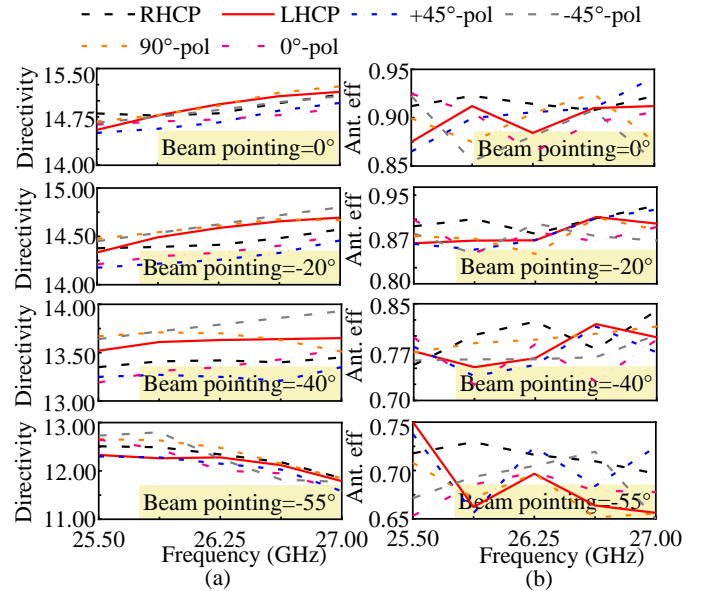

Fig. 21. Simulated directivity and calculated antenna efficiency of the 1×8-element linear phased array at different frequencies (unit of directivity: dBic/dBi). (a) Simulated directivity; (b) antenna efficiency.

by using the unit excitation active element pattern (AEP) method [42], [43]. The measured AEPs of each element for different polarizations are used. The RHCP and LHCP beam scanning performance is given first, as shown in Fig. 18. No grating lobes occur during the beam scanning. For both the RHCP and LHCP, the synthesized beam scanning range reaches ±55° with a gain-reduction of 3.7 dB. The AR for both LHCP and RHCP remain below 3.1 dB. The LP beam scanning performance is given in Fig. 19. Similarly, the range can reach

±55° with a gain-reduction of 4.4 dB. The cross-polarization level rises at an increasing scanning angle, but it is still suppressed by more than 11.2 dB, as shown in Fig. 19(b). Fig. 18(c) and Fig. 19(c) show the top view of the 3-D patterns for each polarization when the beam points to -55°. At large beam scanning angles, good radiation patterns retain.

The simulated and synthesized peak gain at different frequencies are shown in Fig. 20. The maximum variation of the synthesized gain among the different polarizations is about 0.8 dB, which appears at 25.88 GHz with beaming pointing at -40°. This indicates a stable gain reconstruction. During the beam scanning, the synthesized peak gain varies in

TABLE I
3-D RADIATION PATTERNS OF THE 8×8-ELEMRMT PHASED ARRAY
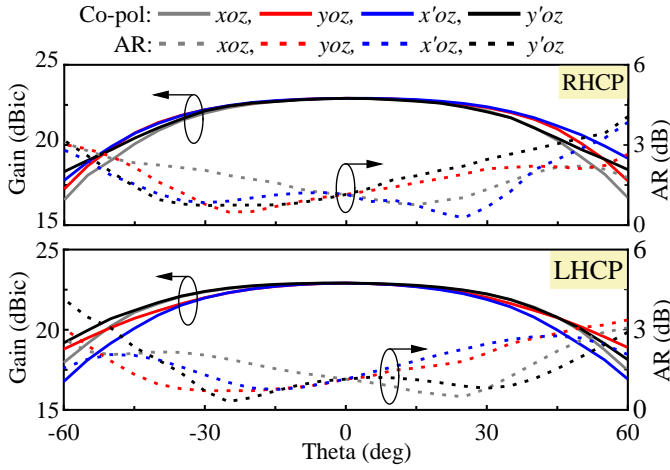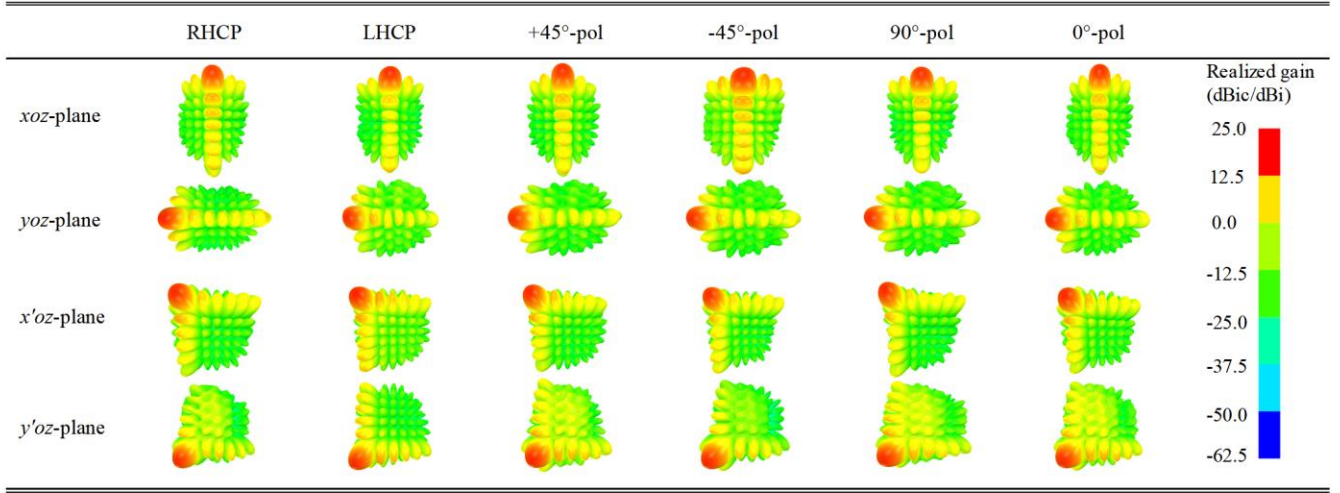
Fig. 22. Simulated CP beam peak gain and AR envelope characteristics of the 8×8-element planar phased array during the beam scanning at 26.25 GHz.

the range of 9.9 - 14.7 dBic/dBi across the operating frequency band. It is about 0.3 - 1.4 dB lower than the simulated result, which is mainly due to the fabrication tolerance, assembly and measurement errors. Fig. 21 plots the simulated directivity and calculated antenna efficiency at different frequencies. The antenna efficiency is calculated from the synthesized peak gain and the simulated directivity. Over the desired frequency range, it is in the range of 65%-94% for all polarizations during beam scanning. From the synthesized peak gain and the array aperture size, the aperture efficiency including the antenna efficiency ($\eta_{ap\times an}$) can be calculated as [44]:

$$\eta_{an\times ap} = \frac{G}{D} \times \frac{D\lambda^2}{4\pi A} = \frac{G\lambda^2}{4\pi A} \tag{5}$$

where G is the realized peak gain, D is the directivity, λ is the free-space wavelength at the operating frequency, and A is the physical array aperture size. This varies from 30% to 87% for all polarizations during the beam scanning.
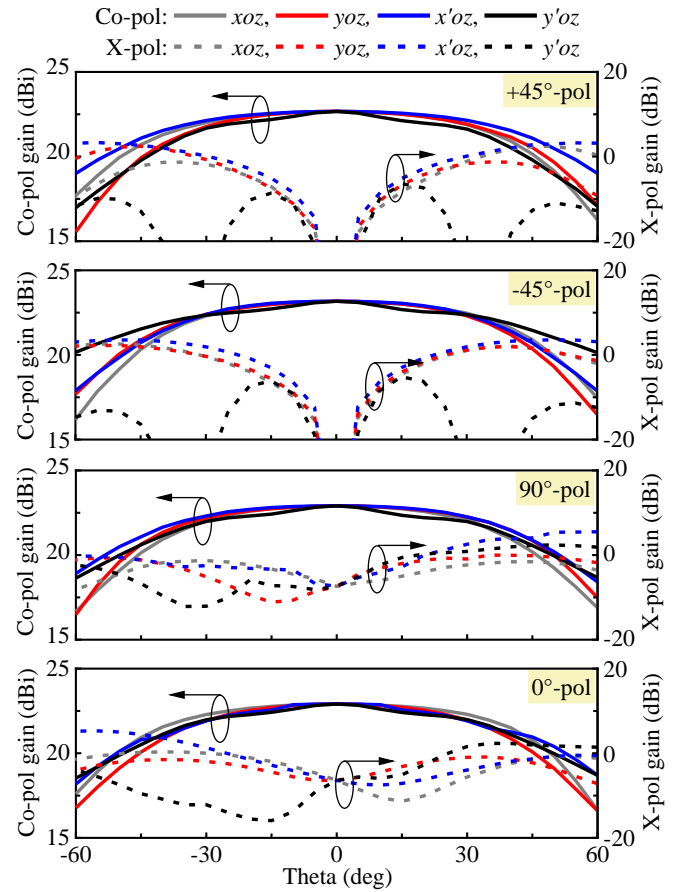
Fig. 23. Simulated LP beam peak gain envelope characteristic of the 8×8-element planar phased array during the beam scanning at 26.25 GHz.

B. 8×8-Element Planar Phased Array

To validate the 2-D beam scanning performance, an 8×8-element phased array is designed and analyzed. The array configuration is shown in Fig. 9(c). The dimensions of each element are the same as those in Fig. 2(d) and (e). The size of the entire phased array is 49 mm × 49 mm. Fig. 22 shows the simulated peak gain and AR envelopes of the main beam

TABLE II
PERFORMANCE COMPARISON OF ALL-METAL PHASED ARRAYS

Ref.	Element type	Freq. (GHz)	Array scale	Scan range	Peak gain[1] (dBic/dBi)	Antenna efficiency (%)	Initial polarization	Profile (λ_0)	T[2]
[25]	Dipole	13.5	16×16	±40°	28.3	90	RHCP	0.31	No
[26]	Dipole	4.7	1×8/4×8	±60°	13.4/17.6	88	Dual LPs	0.11	N.A.
[27]	Vivaldi	11.8	12×20	±45°	/	77	Dual LPs	1.91	N.A.
[28]	Vivaldi	10	8×8	±30°	21	75	Dual LPs	3.47	N.A.
[33]	Frequency-scaled ultra-wide spectrum element	13	12×20	±45°	/	78	Dual LPs	0.39	N.A.
This work	Septum polarizer	26.25	1×8	±55°	14.3	94	Dual CPs	0.46	Yes

[1]It is the peak gain when the beam points to θ=0°. [2]T: Polarization reconfigurability.

(RHCP and LHCP) when the beam is continuously scanning at 26.25 GHz. Considering the practical 2-D beam scanning scenarios, the radiation in *xoz*- and *yoz*-planes, as well as the diagonal planes (*x'oz*- and *y'oz*-planes, marked in Fig. 9(c)), are plotted. Stable beam scanning and AR are achieved in all planes. The beam scanning range reaches ±55° with a gain-reduction of 4.8 dB. During the beam scanning, the simulated AR for both the RHCP and the LHCP remains below 3.4 dB. The simulated peak gain envelope of the main beam for the four synthetic LPs are shown in Fig. 23. It can be observed that each LP can obtain continuous wide-angle scanning up to ±55° (gain drop is less than 5.2 dB) in all four planes, and still has a low XPD of less than 14 dB when the beam points to ±55°. The simulated aperture efficiency including the antenna efficiency is 30% - 90% for all polarizations during the beam scanning. The minimum value occurs at +45°-pol with beam pointing of -55° along *yoz*-plane. TABLE I shows the 3D patterns for each polarization when the beam points to -55°. Good radiation patterns are also maintained at large beam scanning angles.

C. Comparison

The performance comparison of this work with some published all-metal phased arrays is listed in TABLE II. The work in [25] is the single CP phased array, and the works in [26]-[30], [33] are the dual LP phased arrays. The polarization reconfigurability is not discussed in these previous works. We believe our work is the first report of an all-metal phased array with full polarization reconfigurability. Our work also features a simple structure and a reduced profile with competitive beam scanning performance for all polarizations.

IV. CONCLUSION

In this paper, an all-metal phased array with full polarization reconfigurability was demonstrated. A new low-profile miniaturized septum polarizer is devised as the phased array element. It not only ensures the stable CP radiation performance, but also meets the spacing restriction of a phased array. Arbitrary LPs can be synthesized from the orthogonal CP waves generated by the septum polarizer. The 1-D and 2-D beam scanning performance is demonstrated. A prototype

1×8-element phased array covering 25.5 - 27 GHz was fabricated and measured. The feasibility as well as the performance of the proposed phased array have been confirmed. Experimental results show that stable beam scanning performance for both the CPs and LPs. The low complexity, reduced profile, wide-angle scanning, and full polarization reconfigurability make this design a good candidate for metal phased array applications.

REFERENCES

[1] Y. Gou, Y. Chen and S. Yang, "Radar cross section reduction of wideband Vivaldi antenna arrays with array-level scattering cancellation," *IEEE Trans. Antennas Propag.*, vol. 70, no. 8, pp. 6740-6750, Aug. 2022.

[2] H. -T. Chou, "Near-field orthogonal beam scan by phased arrays of antennas with active analog beam former for maximum NF-RCS in target detection," *IEEE Trans. Antennas Propag.*, vol. 70, no. 2, pp. 1559-1564, Feb. 2022.

[3] J. X. Sun, Y. J. Cheng, Y. F. Wu and Y. Fan, "Ultra-wideband, low-profile and low-RCS conformal phased array with capacitance-integrated balun and multi-functional meta-surface," *IEEE Trans. Antennas Propag.*, vol. 70, no. 9, pp. 7448-7457, Sep. 2022.

[4] J. -W. Kim, S. -C. Chae, H. -W. Jo, T. -D. Yeo and J. -W. Yu, "Wideband circularly polarized phased array antenna system for wide axial ratio scanning," *IEEE Trans. Antennas Propag.*, vol. 70, no. 2, pp. 1523-1528, Feb. 2022.

[5] K. -X. Li, Z. -J. Guo and Z. -C. Hao, "A multipolarized planar phased array for LEO SATCOM applications," *IEEE Antennas Wirel. Propag. Lett.*, vol. 21, no. 11, pp. 2273-2277, Nov. 2022.

[6] G. Han, B. Du, W. Wu and B. Yang, "A novel hybrid phased array antenna for satellite communication on-the-move in Ku-band," *IEEE Trans. Antennas Propag.*, vol. 63, no. 4, pp. 1375-1383, Apr. 2015.

[7] H. Cho, H. -W. Jo, J. -W. Kim, K. -S. Kim, J. -I. Oh and J. -W. Yu, "Shorted trapezoidal SIW antenna with quasi-hemispherical pattern for 2D wide scanning planar phased array antenna," *IEEE Trans. Antennas Propag.*, vol. 70, no. 8, pp. 7211-7216, Aug. 2022.

[8] Z. Wang, S. Zhao and Y. Dong, "Miniaturized, vertically polarized, pattern reconfigurable dielectric resonator antenna and its phased array for wide-angle beam-steering," *IEEE Trans. Antennas Propag.*, vol. 70, no. 10, pp. 9233-9246, Oct. 2022.

[9] C. Zhou, W. Yang, Q. Xue, Y. Liu, Y. Xu and W. Che, "Millimeter-wave wideband dual-polarized LTCC antenna array based on metasurfaces for beam-scanning applications," *IEEE Trans. Antennas Propag.*, vol. 70, no. 10, pp. 9912-9917, Oct. 2022.

[10] X. Liu, K. W. Leung, T. Zhang, N. Yang, P. Gu and R. Chen, "An electrically controlled pattern- and polarization-reconfigurable cylindrical dielectric resonator antenna," *IEEE Antennas Wirel. Propag. Lett.*, vol. 20, no. 12, pp. 2309-2313, Dec. 2021.

[11] K. Ghosh and S. Das, "CRLH-TL based reconfigurable antennas with multiple parameter reconfigurability," *IEEE Trans. Antennas Propag.*, vol. 70, no. 7, pp. 5892-5896, Jul. 2022.

[12] G. Mishra and S. K. Sharma, "A multifunctional full-polarization reconfigurable 28 GHz staggered butterfly 1-D-beam steering antenna," *IEEE Trans. Antennas Propag.*, vol. 69, no. 10, pp. 6468-6479, Oct. 2021.

[13] Y. -Q. Wen, S. Gao, B. -Z. Wang and Q. Luo, "Dual-polarized and wide-angle scanning microstrip phased array," *IEEE Trans. Antennas Propag.*, vol. 66, no. 7, pp. 3775-3780, Jul. 2018.

[14] G. Gao, X. Ding, Y. Cheng and W. Shao, "Dual-polarized wide-angle scanning phased array based on multimode patch elements," *IEEE Antennas Wirel. Propag. Lett.*, vol. 18, no. 3, pp. 546-550, Mar. 2019.

[15] X. Luo et al., "A scalable Ka-band 1024-element transmit dual-circularly-polarized planar phased array for SATCOM application," *IEEE Access*, vol. 8, pp. 156084-156095, 2020.

[16] M. Mirmozafari, S. Saeedi, G. Zhang and Y. Rahmat-Samii, "A crossed dipole phased array antenna architecture with enhanced polarization and isolation characteristics," *IEEE Trans. Antennas Propag.*, vol. 68, no. 6, pp. 4469-4478, Jun. 2020.

[17] H. Zhang, S. Yang, Y. Chen, J. Guo and Z. Nie, "Wideband dual-polarized linear array of tightly coupled elements," *IEEE Trans. Antennas Propag.*, vol. 66, no. 1, pp. 476-480, Jan. 2018.

[18] S. J. Yang, Y. M. Pan, Y. Zhang, Y. Gao and X. Y. Zhang, "Low-profile dual-polarized filtering magneto-electric dipole antenna for 5G applications," *IEEE Trans. Antennas Propag.*, vol. 67, no. 10, pp. 6235-6243, Oct. 2019.

[19] B. Feng, J. Chen, K. L. Chung, L. Wang and Y. Li, "Dual-polarized filtering magneto-electric dipole antenna arrays with high radiation-suppression index for 5G new radio n258 operations," *IEEE Trans. Antennas Propag.*, vol. 70, no. 4, pp. 3058-3063, Apr. 2022.

[20] H. -T. Chou, S. -J. Chou, J. D. S. Deng, C. -H. Chang and Z. -D. Yan, "LTCC-based antenna-in-package array for 5G user equipment with dual-polarized endfire radiations at millimeter-wave frequencies," *IEEE Trans. Antennas Propag.*, vol. 70, no. 4, pp. 3076-3081, Apr. 2022.

[21] A. A. Omar et al., "A planar, polarization-switchable endfire and ±broadside millimeter-wave antenna array without lumped components," *IEEE Trans. Antennas Propag*., vol. 70, no. 5, pp. 3864-3869, May 2022.

[22] K. K. W. Low, S. Zihir, T. Kanar and G. M. Rebeiz, "A 27–31-GHz 1024-element Ka-band SATCOM phased-array transmitter with 49.5-dBw peak EIRP, 1-dB AR, and ±70° beam scanning," *IEEE Trans. Microwave Theory Tech.*, vol. 70, no. 3, pp. 1757-1768, Mar. 2022.

[23] A. H. Aljuhani, T. Kanar, S. Zihir and G. M. Rebeiz, "A 256-element Ku-band polarization agile SATCOM receive phased array with wide-angle scanning and high polarization purity," *IEEE Trans. Microwave Theory Tech.*, vol. 69, no. 5, pp. 2609-2628, May 2021.

[24] M. Sano, M. Higaki, K. Wada and K. Hashimoto, "A patch antenna array with a rotatable polarization plane for Ku-band phased arrays," *2020 International Symposium on Antennas and Propagation (ISAP)*, pp. 7-8, Jan. 2021.

[25] L. -K. Zhang, Y. -X. Wang, J. -Y. Li, Y. Feng and W. Zhang, "Cavity-backed circularly polarized cross-dipole phased arrays," *IEEE Antennas Wirel. Propag. Lett.*, vol. 20, no. 9, pp. 1656-1660, Sep. 2021.

[26] G. Yang and S. Zhang, "Dual polarized wide-angle scanning phased array antenna for 5G communication system," *IEEE Trans. Antennas Propag*., vol. 70, no. 9, pp. 7427-7438, Sep. 2022.

[27] R. W. Kindt and B. T. Binder, "Dual-polarized Vivaldi array on a triangular lattice," *IEEE Trans. Antennas Propag.*, vol. 69, no. 4, pp. 2083-2091, Apr. 2021.

[28] J. -B. Yan, S. Gogineni, B. Camps-Raga and J. Brozena, "A dual-polarized 2–18-GHz Vivaldi array for airborne radar measurements of snow," *IEEE Trans. Antennas Propag.*, vol. 64, no. 2, pp. 781-785, Feb. 2016.

[29] H. Kähkönen, J. Ala-Laurinaho and V. Viikari, "A modular dual-polarized Ka-band Vivaldi antenna array," *IEEE Access*, vol. 10, pp. 36362-36372, 2022.

[30] M. A. Elmansouri, G. R. Friedrichs, L. B. Boskovic and D. S. Filipovic, "An X-band through Ka-band thinned all-metal Vivaldi phased array,"

[31] D. T. McGrath, N. Schuneman, T. H. Shively and J. Irion, "Polarization properties of scanning arrays," *in Proc. IEEE Int. Symp. Phased Array Syst. Technol.*, Oct. 2003, pp. 295-299.

[32] D. H. Schaubert, J. Shin, and G. Wunsch, "Characteristics of single polarized phased array of tapered slot antennas," *in Proc. Int. Symp. Phased Array Syst. Technol.*, Boston, MA, 1996, pp. 102–106.

[33] R. W. Kindt and B. T. Binder, "Wideband, low-profile, dual-polarized machined-metal array on a triangular lattice," *IEEE Trans. Antennas Propag.*, vol. 70, no. 2, pp. 1097-1106, Feb. 2022.

[34] M. Sano and M. Higaki, "A linearly polarized patch antenna with a continuously reconfigurable polarization plane," *IEEE Trans. Antennas Propag.*, vol. 67, no. 8, pp. 5678-5683, Aug. 2019.

[35] J. Wu, Y. J. Cheng, H. B. Wang, Y. C. Zhong, D. Ma and Y. Fan, "A wideband dual circularly polarized full-corporate waveguide array antenna fed by triple-resonant cavities," *IEEE Trans. Antennas Propag.*, vol. 65, no. 4, pp. 2135-2139, Apr. 2017.

[36] Ming Chen and G. Tsandoulas, "A wide-band square-waveguide array polarizer," *IEEE Trans. Antennas Propag.*, vol. 21, no. 3, pp. 389-391, May 1973.

[37] J. Angevain and N. J. G. Fonseca, "Waveguide septum polarizer shaped with legendre polynomials," *in Proc. 11th Eur. Conf. Antennas Propag. (EuCAP)*, Paris, France, Mar. 2017, pp. 2286-2290.

[38] R. Mailloux, Phased Array Antenna Handbook, 2nd ed. Norwood, MA, USA: Artech House, 2005.

[39] Y. -M. Yang, C. -W. Yuan and B. -L. Qian, "A novel phase shifter for Ku-band high-power microwave applications," *IEEE Trans. Plasma Sci*, vol. 42, no. 1, pp. 51-54, Jan. 2014.

[40] J. X. Sun, Y. J. Cheng and Y. Fan, "Planar ultra-wideband and wide-scanning dual-polarized phased array with integrated coupled-marchand balun for high polarization isolation and low cross-polarization," *IEEE Trans. Antennas Propag.,* vol. 69, no. 11, pp. 7134-7144, Nov. 2021.

[41] D. M. Pozar, "The active element pattern," *IEEE Trans. Antennas Propag.*, vol. 42, no. 8, pp. 1176-1178, Aug. 1994.

[42] Z. -L. Su, K. W. Leung and K. Lu, "A shaped-beam antenna for wide-angle scanning phased array," *IEEE Trans. Antennas Propag.*, vol. 70, no. 9, pp. 7659-7669, Sept. 2022.

[43] Y. Li and S. Xiao, "Wideband wide-angle scanning phased array based on miniaturized metasurface antenna," *IEEE Trans. Antennas Propag.*, vol. 70, no. 2, pp. 1107-1119, Feb. 2022.

[44] C. A. Balanis, *Antenna Theory: Analysis and Design.* Hoboken, NJ, USA: Wiley, 2005.

IEEE Trans. Antennas Propag., vol. 69, no. 11, pp. 7613-7623, Nov. 2021.